# Nanometer-level stitching in raster-scanning electron-beam lithography using spatial-phase locking

J. T. Hastings,[a] Feng Zhang, and Henry I. Smith[b]
*Department of Electrical Engineering and Computer Science, Massachusetts Institute of Technology, Cambridge, Massachusetts 02139*

(Received 8 July 2003; accepted 8 September 2003; published 4 December 2003)

Pattern-placement inaccuracy is a persistent problem in scanning-electron-beam lithography (SEBL) despite the high-resolution obtained in SEBL systems. Pattern-placement errors stem from a variety of environmental and system variations; however, the fundamental issue is the open-loop nature of the system, i.e., the beam location on the substrate is not monitored during exposure. In contrast, spatial-phase-locked electron-beam lithography (SPLEBL) provides closed-loop control of the beam position by monitoring the signal from a fiducial grid on the substrate. By detecting the spatial phase of the grid signal one can estimate the beam position within a small fraction of the grid period. We have implemented SPLEBL by adding real-time signal processing, feedback control, and raster-scan exposure capability to an inexpensive SEBL system. Using a 246 nm period, electron-transparent fiducial grid that covers the entire substrate, we have exposed patterns that exhibit global placement accuracy with respect to the grid and field-stitching precision better than 1.3 nm (one standard deviation). © *2003 American Vacuum Society.* [DOI: 10.1116/1.1622944]

## I. INTRODUCTION

Scanning electron-beam lithography (SEBL) provides arbitrary pattern generation with sub-10 nm resolution. However, system imperfections, environmental disturbances, charging, and a variety of other factors limit SEBL's pattern-placement accuracy to tens of nanometers. This level of placement accuracy remains inadequate for integrated-circuit mask writing beyond the 45 nm technology node, even with 4× demagnification.[1] Imprint and proximity x-ray lithographies require 1× masks with even more stringent placement tolerances. In addition, photonic devices, which typically rely on optical interference, require features be placed accurately within a small fraction of the wavelength of light. The requirements for such devices often exceed current SEBL tool capabilities.[2–4]

The inadequacy of SEBL pattern placement arises from the fundamentally open-loop nature of conventional systems. While the position of the stage is precisely measured with a laser interferometer, the actual e-beam location is not monitored during pattern exposure. Any undesired displacement between the e-beam and the substrate, or between the substrate and the stage, results in pattern error. To combat these errors one must precisely control the vibration, stray fields, temperature, interferometer-mirror flatness, deflection distortion, and many other system variables. Such control leads to inordinately complicated costly tools.

Several techniques improve pattern placement at the expense of exposure time. Frequently referencing fiducial marks on the interferometer-controlled stage can compensate for a slow beam or substrate drift, but the time required to move the stage and image these marks reduces throughput. Multiple exposures of the same pattern effectively ''average'' placement errors, but also at the expense of throughput and linewidth control.[5] Finally, one can correct certain repeatable, pattern-dependent errors by exposing test substrates, measuring systematic errors, and correcting them in subsequent exposures, but this approach greatly increases the time required to produce the final pattern, and these corrections may not be stable over time. Although helpful, these techniques do not offer a means of locating the beam on the sample *during* the pattern exposure, nor have they achieved sub-10 nm placement accuracy to date.

Spatial-phase-locked electron-beam lithography (SPLEBL), shown schematically in Fig. 1, dramatically improves pattern placement by providing closed-loop control of the beam position. During pattern exposure, one detects a periodic signal produced by the interaction of the e-beam with a fiducial grid on the substrate. Measuring the spatial phase of this signal allows estimation of the beam-placement error within a small fraction of the grid period. Fiducial grids with long-range spatial-phase coherence and periods as small as 200 nm can be produced by interference lithography[6] or scanning-beam interference lithography.[7]

We have implemented SPLEBL on MIT's Raith-150 SEBL system using continuous feedback to correct pattern-placement errors. Custom hardware and software provide real-time spatial-phase locking, raster-scan pattern exposure, and correction of deflection nonlinearities. The system uses an electron-transparent fiducial grid placed on top of the e-beam resist. Because the grid covers the entire substrate, and beam-placement corrections are supplied continuously, the technique does not adversely affect throughput. Patterns exposed with this system exhibit global placement accuracy with respect to the grid and field-stitching errors with standard deviations below 1.3 nm.

[a]Currently at Department of Electrical and Computer Engineering, University of Kentucky, Lexington, KY.
[b]Electronic mail: hismith@nano.mit.edu

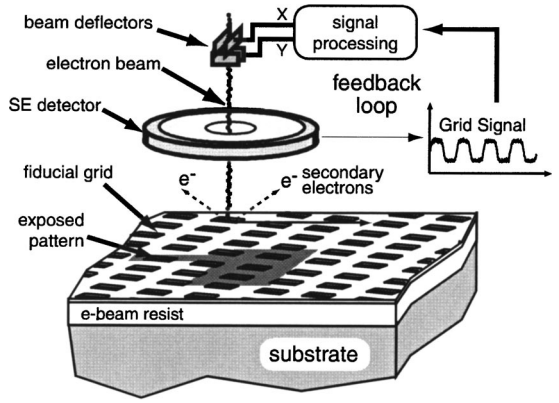


FIG. 1. Schematic diagram of real-time spatial-phase-locked electron-beam lithography. As the e-beam raster scans across the substrate the periodic signal from an electron-transparent grid is used to provide feedback control of the beam position. The fiducial grid consists of a thin, metal lattice placed on the e-beam resist that provides contrast in the secondary-electron signal. The grid covers the entire substrate and is rotated at an angle with respect to the raster-scan direction so that both *x*- and *y*-placement errors are corrected simultaneously.

## II. REAL-TIME SPATIAL-PHASE LOCKING

Previous spatial-phase locking implementations measured the spatial phase of the grid intermittently and then exposed the pattern normally, i.e., open loop.[4,8–10] In these approaches phase locking is typically performed before exposing each deflection field in a vector-scan system. These ''look-then-write'' techniques have shown excellent results, but are limited by the stability of the system during exposure and by pattern-dependent errors. In addition, the time required to lock to the grid before exposing each field reduces throughput. To overcome these limitations, we developed and implemented a real-time approach to spatial-phase locking that provides continuous feedback throughout the exposure.

Although one can conceive of continuous spatial-phase locking techniques for vector-scan systems, raster-scan exposure provides the most direct implementation. Scanning the beam in a regular fashion produces a simple, periodic signal. In addition, one would like to monitor the grid signal with a subexposure-dose beam current while scanning nonexposed regions, and switch to a higher-current beam when exposure is desired. In this way, the grid signal would be always available to the phase-locking system. Currently, we do not have this dose-modulation capability in our SEBL system; however, a patterning approach that circumvents this restriction is described in Sec. V.

To perform SPLEBL we must extract the beam-placement error from the grid signal. We model the signal as a sum of geometrically orthogonal sinusoids that represent the grid's fundamental spatial-frequency components. If the faster raster-scan direction, assumed here to be *x*, is oriented along the grid axes, it is necessary to scan several lines before estimating the *y*-axis placement error. However, if the grid is rotated by an angle, $\theta$, with respect to the scan direction, as shown in Fig. 2(a), we can simultaneously obtain information about the beam's *x* and *y* displacement.

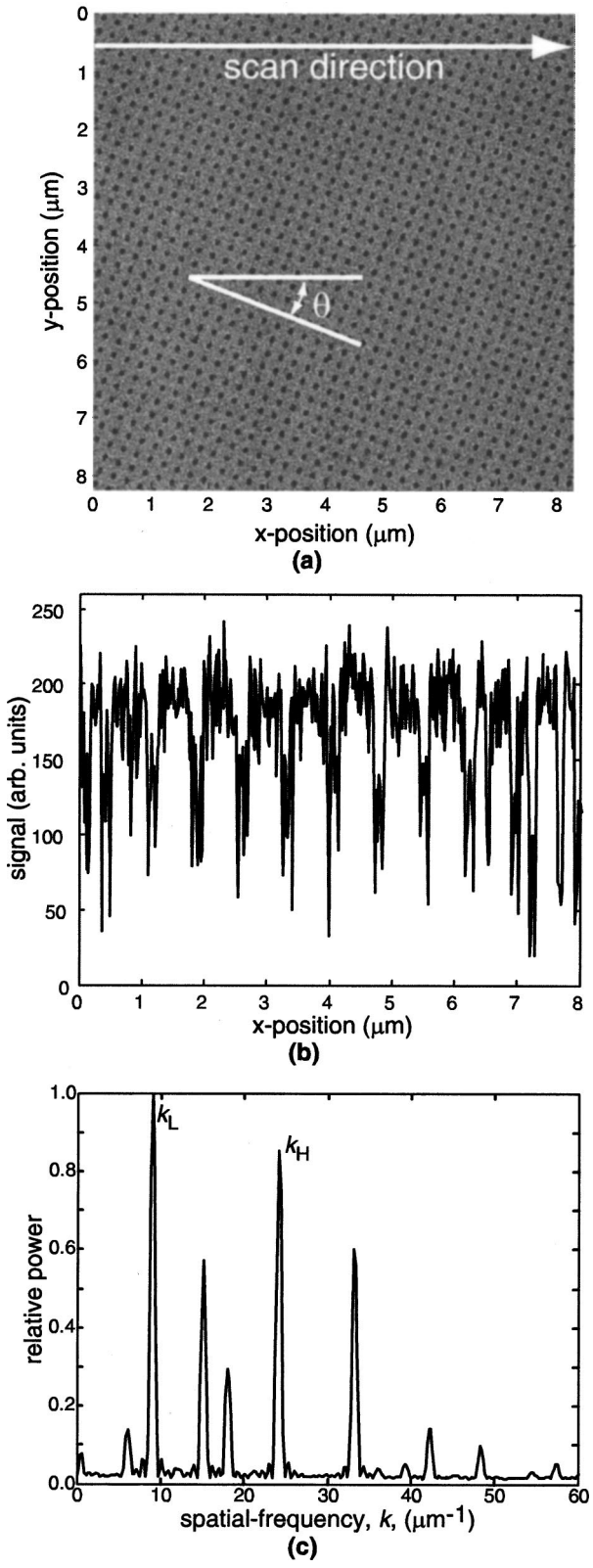


FIG. 2. (a) Scanning-electron micrograph of a 246 nm period, 8 nm thick, aluminum-fiducial grid used for spatial-phase locking. The grid is rotated with respect to the raster-scan direction to simultaneously provide *x*- and *y*-axis beam-deflection correction. (b) Secondary-electron signal from the grid shown in (a). (c) Spatial-frequency power spectrum of the secondary-electron signal shown in (b) (averaged over 512 scans). The fundamental spatial-frequency components, $k_L$ and $k_H$, are labeled. The other components represent harmonics and sum and difference frequencies.

If the e-beam strikes a rotated grid with period $\Lambda_G$ at location $(x_B, y_B)$ the signal, $S$, is given by

$$S(x_B, y_B) = a\cos[k_0(x_B\cos\theta + y_B\sin\theta)] + a\cos[k_0(y_B\cos\theta - x_B\sin\theta)], \quad (1)$$

where the grid's spatial frequency is $k_0 = 2\pi/\Lambda_G$, and the amplitude of each sinusoid is $a$. The beam's position can be described in terms of the desired position $(x_P, y_P)$ and the placement errors, $\Delta x$ and $\Delta y$. Thus,

$$x_B = x_P + \Delta x \quad (2)$$

and

$$y_B = y_P + \Delta y. \quad (3)$$

If we substitute Eqs. (2) and (3) in Eq. (1), and take the Fourier transform with respect to $x_P$, we find that

$$F_x(k, y_P) = \frac{a}{2}\delta(k \pm k_0\cos\theta)\exp[\pm jk_0(\Delta x\cos\theta + \Delta y\sin\theta + y_P\sin\theta)] + \frac{a}{2}\delta(k \pm k_0\sin\theta)\exp[\mp jk_0(-\Delta x\sin\theta + \Delta y\cos\theta + y_P\cos\theta)]. \quad (4)$$

We obtain positive high and low spatial-frequency components: $k_H = k_0\cos\theta$ and $k_L = k_0\sin\theta$.

Figure 2(b) shows the secondary-electron signal from the rotated grid, made of 8-nm-thick aluminum, in Fig. 2(a). Figure 2(c) shows the spatial-frequency spectrum, averaged over 512 scans, of the rotated grid signal. Although the signal from the aluminum grid exhibits higher harmonics and sum and difference frequencies, the fundamental components, $k_L$ and $k_H$, are easily identified.

The last term of each exponential in Eq. (4) is determined by $\theta$ and $y_P$, both of which are known for any given measurement. These terms lead to deterministic phase progressions of the high- and low-frequency components as the beam progresses in the $y$ direction. Thus, we can subtract this phase offset and measure only the phase-error terms, $\Delta\phi_H$ and $\Delta\phi_L$, given by

$$\Delta\phi_H = k_0(\Delta x\cos\theta + \Delta y\sin\theta) \quad (5)$$

and

$$\Delta\phi_L = -k_0(-\Delta x\sin\theta + \Delta y\cos\theta). \quad (6)$$

We calculate the $x$ and $y$ shifts by solving these equations for $\Delta x$ and $\Delta y$:

$$\Delta x = (\Delta\phi_H\cos\theta + \Delta\phi_L\sin\theta)/k_0 \quad (7)$$

and

$$\Delta y = (\Delta\phi_H\sin\theta - \Delta\phi_L\cos\theta)/k_0. \quad (8)$$

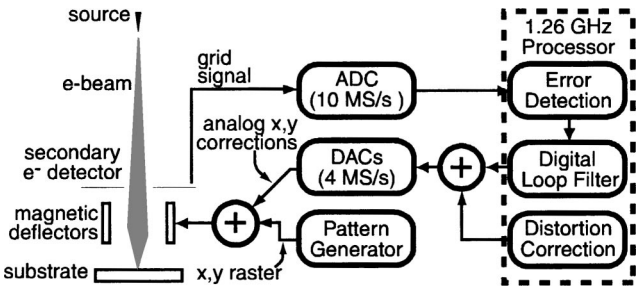


FIG. 3. Block diagram of spatial-phase locking implemented on MIT's Raith-150 SEBL system. The feedback loop consists of the secondary-electron detector, a 10 MS/s ADC, a dedicated microprocessor running a real-time operating system, and two 4 MS/s DACs. The beam-placement error estimation algorithm and a digital loop filter are implemented in software on the microprocessor. The Raith-150 pattern generator raster scans the beam across the field, and deflection nonlinearities are corrected through third order by adding the required $x$- and $y$-deflection signals.

Thus, by performing phase locking at two frequencies, we can correct both $x$- and $y$-placement errors.

It might seem that locking to a rotated grid will provide better phase-locking precision for one axis than the other. However, this is not the case if one samples several periods for each spatial frequency, satisfies the Nyquist criterion, and uses an efficient estimator, such as the discrete-Fourier transform, to determine the phase errors. If these conditions are met, the variance of the phase estimates depends only on the signal-to-noise ratio and the number of samples acquired. Thus, most rotation angles provide good phase locking, but one must remember that $k_L$ approaches zero for small angles and the discrete Fourier transform is no longer an efficient estimator. When $\theta$ approaches 45° both $k_L$ and $k_H$ approach $\sqrt{2}k_0/2$ and we observe interference between the phase estimates.

Noise in the grid signal prevents perfect phase estimation; as a result, we filter the correction signals, $\Delta x$ and $\Delta y$, before applying feedback to the beam-deflection system. The loop filter, shown in the system diagram of Fig. 3, allows one to trade-off frequency response and locking precision in the feedback loop. Optimal filter selection minimizes beam-positioning error by balancing contributions from physical disturbances and phase-estimation error.

Figure 3 illustrates the real-time spatial-phase locking system. We implemented the algorithm described above in software on a dedicated Pentium 1.26 GHz microprocessor (National Instruments model PXI-8176) running the LabView RealTime operating system. The secondary-electron signal from the fiducial grid was sampled using a 10 megasamples per second (MS/s) analog-to-digital converter (ADC) on a National Instruments PXI-6115 multipurpose input/output (I/O) board. After processing the grid signal, two 4 MS/s digital-to-analog converters (DAC) on the PXI-6115 board were used to feed back the $x$- and $y$-deflection corrections to the Raith-150 system.

## III. RASTER-SCAN PATTERN EXPOSURE

The algorithm described in Sec. II is best suited for a raster-scan exposure strategy. MIT's Raith-150 SEBL system

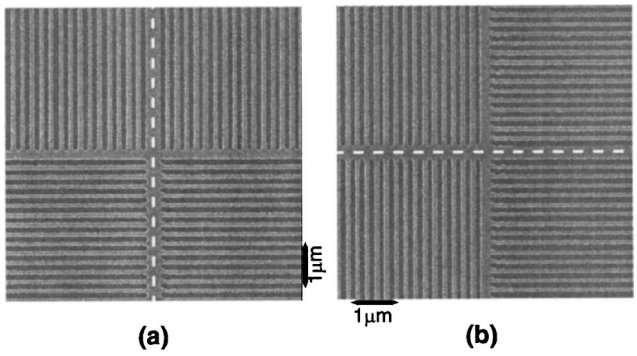


FIG. 4. Scanning-electron micrographs of 200 nm period PMMA gratings exposed using a raster-scan strategy with real-time spatial-phase locking. The images encompass the boundaries between stitched deflection fields. The dashed lines indicate the vertical (a) and horizontal (b) field boundaries.

was designed for vector-scan operation, but we modified the system to conduct raster-scan exposures. In most raster-scan systems the beam scans rapidly in one direction while the stage scans along the orthogonal direction. In our implementation the stage remains stationary while the beam deflection system scans the beam along both the fast axis, *x*, and the slow axis, *y*.

To perform raster-scan exposures with the Raith-150, the pattern generator scans the beam over the entire field while supplemental hardware and software control the electrostatic beam blanker. A digital input/output board, model PCI-6534 (National Instruments, Natick, MA), was added to the Raith system's computer to supply the beam-blanker control signal. The board provides continuous digital output at up to 20 Mb/s per channel, which is sufficient for the pattern generator's 10 MHz maximum pixel-address rate. We developed software to supply the I/O board with data based on GDS-II pattern files. As the beam scans over the field, the beam-blanker data stream is generated in nearly real-time to reduce pattern-conversion overhead time.

Accurate pattern placement requires synchronization of the beam blanker and the beam deflectors. The pattern generator steps the beam from pixel to pixel based on a variable-period clock, and this clock synchronizes the beam blanker with the deflection system. This pixel clock is based on a variable oscillator (11.111–16.666 MHz) that is multiplied and divided within the pattern-generator's microprocessor to obtain the desired pixel dwell time.[11] We reproduce and distribute the pixel-clock signal to the beam-blanker controller and the spatial-phase locking system using a modified Cypress Semiconductor (San Jose, CA) CY30700 programmable clock board.

This modified Raith-150 produces high-fidelity patterns, including the 200 nm period gratings shown in Fig. 4. These patterns were written in raster-scan mode using a 10 keV e-beam and a dose of 70 $\mu$C/cm$^2$. The pixel clock was 2.469 MHz and the address-grid size was 10 nm. Although the raster-scan pattern generator is capable of boustrophedonic scanning (alternately scanning left to right and right to left), these patterns were exposed by scanning only from left to right. The vertical pattern edges, perpendicular to the scan direction, show excellent fidelity. This is to be expected because the blanker rise and fall times are specified as less than 50 ns, or ≈12% of the dwell time.[11] The horizontal pattern edges exhibit slight modulation in the area immediately after the beam is turned on. It appears that the beam shifts along the *y* direction when it unblanks. This is presumably caused by ringing of the circuit formed by the blanker plates and the associated wiring and power supply. This problem occurs over a time scale too short to be corrected with spatial-phase locking, so the blanker itself needs improvement. This problem has been observed in commercial mask-writing systems,[12] and is presumably largely solved to meet existing mask specifications.

## IV. HIGHER-ORDER DISTORTION CORRECTION

Raster-scan experiments with the Raith-150 revealed field distortions that are not well characterized by first-order (scale, rotation, and shift) parameters. These higher-order distortions must be minimized to achieve nanometer-level pattern placement. Scanning over the fiducial grid is an excellent way to measure these errors, and one would hope to correct them using spatial-phase locking. Unfortunately, some of the distortions cause the beam-position error to vary too rapidly across the field for our current phase-locking system to correct. As a result, we measure these distortions with respect to the fiducial grid, and then add the appropriate corrections to the feedback signal while exposing each field. The distortions need be measured only once per substrate, so the overhead time for this procedure is negligible.

To improve deflection distortion in the Raith-150 system we implemented correction through third order with 10 terms per axis. This is accomplished by relating the desired beam position $(x_P, y_P)$ and the actual beam position $(x_B, y_B)$ with two-dimensional polynomials.

$$x_B = a_0 + a_1 x_P + a_2 y_P + a_3 x_P y_P + a_4 x_P^2 + a_5 y_P^2 + a_6 x_P^3 + a_7 y_P^3 + a_8 x_P^2 y_P + a_9 x_P y_P^2, \tag{9}$$

$$y_B = b_0 + b_1 x_P + b_2 y_P + b_3 x_P y_P + b_4 x_P^2 + b_5 y_P^2 + b_6 x_P^3 + b_7 y_P^3 + b_8 x_P^2 y_P + b_9 x_P y_P^2, \tag{10}$$

where the coefficients $a_0, \ldots, a_9$ and $b_0, \ldots, b_9$ specify the deflection distortion. Typically, one would estimate the coefficients in Eqs. (9) and (10) by moving the stage to at least 10 different positions, deflecting the beam to image a fiducial mark, and measuring the deviation of the mark image from its expected position.[13] This slow procedure is unnecessary with spatial-phase locking available. By disabling the feedback signals to the deflection system, and recording the beam-placement error with respect to the grid throughout the field, one can calculate the coefficients above after a single raster scan.

In our implementation, we divide the deflection field into a 10×10 array of square regions. For a 100 $\mu$m field each of these regions is 10 $\mu$m on a side, and, if the address grid is

10 nm, each region contains 1000×1000 samples of the grid signal. Calculating the average beam-placement error in each of these regions provides a map of the field distortion after a single raster scan. Figure 5(a) shows the residual distortion after correcting only the shift, scale, and rotation. The outermost distortion measurements are not shown in order to make the center region clearer. The extreme distortion at the left edge of the field is induced by the beam "fly back" between each line.

Once a distortion map has been constructed one can calculate the correction coefficients with a least-squares solution to the following matrix equation:

$$\begin{bmatrix} x_{B1} \\ x_{B2} \\ x_{B3} \\ \vdots \\ x_{B100} \end{bmatrix} = \begin{bmatrix} 1 & x_{P1} & y_{P1} & x_{P1}y_{P1} & x_{P1}^2 & y_{P1}^2 & x_{P1}^3 & y_{P1}^3 & x_{P1}^2y_{P1} & x_{P1}y_{P1}^2 \\ 1 & x_{P2} & y_{P2} & x_{P2}y_{P2} & x_{P2}^2 & y_{P2}^2 & x_{P2}^3 & y_{P2}^3 & x_{P2}^2y_{P2} & x_{P2}y_{P2}^2 \\ 1 & x_{P3} & y_{P3} & x_{P3}y_{P3} & x_{P3}^2 & y_{P3}^2 & x_{P3}^3 & y_{P3}^3 & x_{P3}^2y_{P3} & x_{P3}y_{P3}^2 \\ & & & & & \vdots & & & & \\ 1 & x_{P100} & y_{P100} & x_{P100}y_{P100} & x_{P100}^2 & y_{P100}^2 & x_{P100}^3 & y_{P100}^3 & x_{P100}^2y_{P100} & x_{P100}y_{P100}^2 \end{bmatrix} \begin{bmatrix} a_0 \\ a_1 \\ a_2 \\ a_3 \\ a_4 \\ a_5 \\ a_6 \\ a_7 \\ a_8 \\ a_9 \end{bmatrix}. \quad (11)$$

The coefficients for $y$-deflection correction, $b_0,\ldots,b_9$, can be calculated in the same way. These coefficients are stored for the duration of the exposure and the appropriate corrections are added to the feedback signal, shown in Fig. 3, as the beam scans over the field. Figure 5(b) shows a sample distortion map after applying third-order corrections. The distortion in the center 80 $\mu$m of the field has been reduced below 2 nm.

## V. FIELD-STITCHING EXPERIMENTS

After implementing the real-time spatial-phase-locking algorithm with raster-scan exposure and third-order distortion correction, we conducted field-stitching experiments to assess the effectiveness of real-time spatial-phase locking. Using a thin, electron-transparent, aluminum gird, we exposed arrays of 200 nm period gratings with stitching errors below 1.3 nm ($1\sigma$). In addition, every feature is placed with respect to the fiducial grid, so long-range pattern placement exhibits comparable precision.

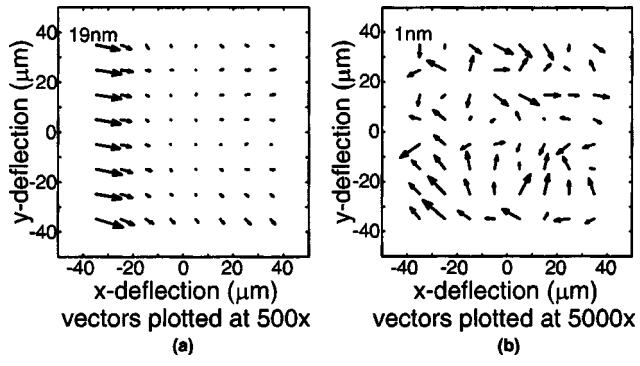


FIG. 5. Raster-scan deflection-field distortion maps. The vectors represent the mean difference between the intended and actual beam positions for each region of the field. (a) Residual distortion after applying first-order (shift, scale, and rotation) corrections. Vectors are magnified 500 times with respect to the axes. (b) Residual distortion after applying third-order corrections. Vectors are magnified 5000 times with respect to the axes.

An 8-nm-thick, 246 nm period, aluminum lattice, shown in Fig. 2(a), served as the fiducial grid for the real-time spatial-phase-locking experiments. Silicon substrates were coated with 100 nm of XHRiC (Brewer Science, Rolla, MO) antireflection coating (ARC), 120 nm of 950 K molecular weight polymethylmethacrylate (PMMA) e-beam resist, 8 nm of evaporated $SiO_x$ and 250 nm of Sumitomo PFI-88 (Tokyo, Japan) positive photoresist. The PFI-88 was exposed with interference lithography using a Lloyd mirror[14] interferometer and a 325 nm wavelength HeCd laser. Two orthogonal exposures produced an array of photoresist posts, and an 8-nm-thick aluminum layer was electron-beam evaporated onto the sample. The PFI-88 resist was removed with isopropyl alcohol (IPA) so that the aluminum lattice remained. Mirror nonflatness and spurious scattering limit the spatial-phase coherence of grids patterned with the Lloyd mirror interferometer; therefore, one would not use such an interferometer for critical masks or devices. However, the Lloyd mirror provides rapid and convienient process development and the resulting grids are adequate for testing spatial-phase locking.

The substrates described above were loaded into the Raith-150 system at an angle of approximately $-0.353$ rad with respect to the laser-interferometer controlled stage's axes. The stage controls were calibrated to move along axes rotated $-0.352\,990$ rad with respect to the grid. Because we have not implemented a dose-modulation scheme in the Raith system, a test pattern was chosen in which the beam remains on during almost the entire field exposure. This pat-

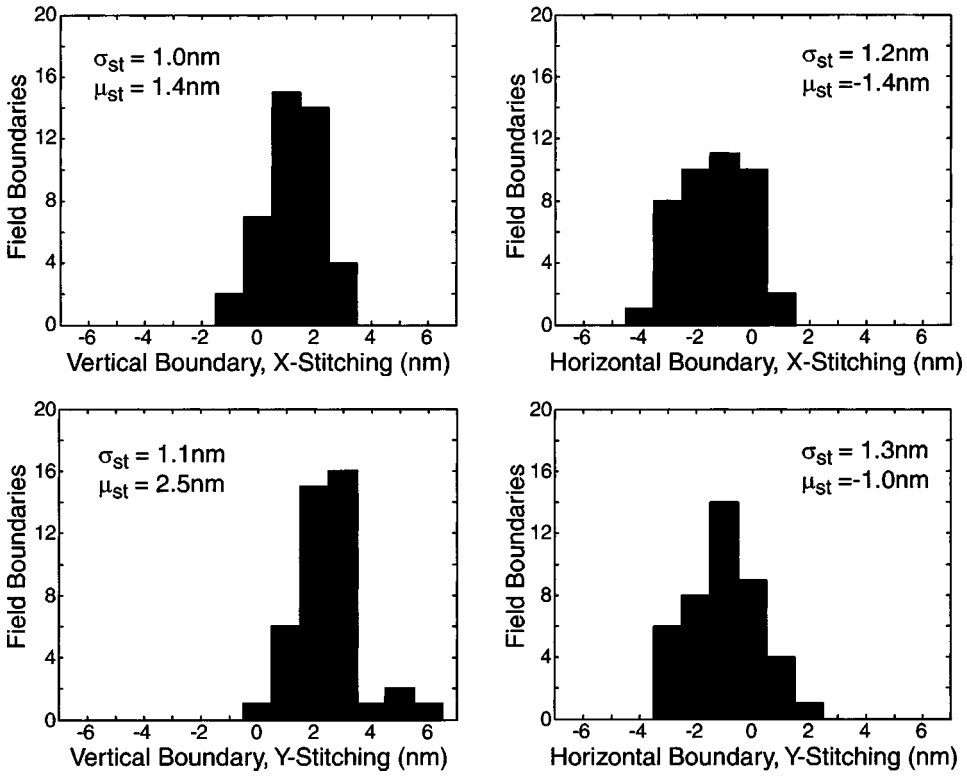


FIG. 6. Histograms of field-stitching errors obtained with real-time spatial-phase locking. Both *x*- and *y*-stitching errors are shown for the horizontal and vertical field boundaries. The errors' means, $\mu_{st}$, and standard deviations, $\sigma_{st}$, are listed for each histogram.

tern consists of 200 nm period vertical and horizontal gratings at each field boundary; however, instead of exposing the grating lines themselves, we expose the entire surrounding area. After development, PMMA remains in regions where the beam was briefly turned off.

The test pattern was isolated to a $60\times60$ $\mu$m region of the field where $-20\,\mu\text{m}\leqslant x\leqslant 40\,\mu\text{m}$ and $-30\,\mu\text{m}\leqslant y\leqslant 30\,\mu\text{m}$. Although the third-order distortion correction removes the mean displacement error over a larger area, these corrections are currently updated too infrequently. At the left edge of the field, when the beam begins its scan, errors within the 10 $\mu$m correction regions change by several nanometers. Thus, we decided to restrict the pattern to a region with sub-1 nm quantization error. Patterning larger regions of the field will be possible after software revision for more frequent distortion correction.

Using spatial-phase locking, we exposed arrays of $7\times7$ fields with the gratings at the edge of each field aligned to those in the adjacent fields. The signal from the aluminum fiducial grid was acquired using the Raith system's in-lens secondary-electron detector. Before starting the exposure we scanned the fiducial grid and calculated the first-order field-correction coefficients (scale, rotation, and shift). These corrections were applied with the Raith field-correction hardware. Then we scanned the grid two more times and calculated corrections through third order. These corrections were applied simultaneously with the spatial-phase-locking corrections.

For these exposures a simple integrator was used for the digital-loop filter. The gain was chosen to keep estimation errors in the correction signal below 1 nm, but this limited the 3 dB bandwidth of the correction signals to $\approx$2 Hz. For the first four lines (40 nm) of the field the gain was increased by a factor of 16 to more rapidly correct the initial placement error present after each field-to-field stage movement. Improving the grid's signal-to-noise ratio (SNR) and increasing the pixel rate will improve both the feedback correction bandwidth and precision.

After exposing the grating patterns we removed the aluminum grid and the $SiO_x$ interlayer using a buffered hydrofluoric acid solution. We developed the PMMA in a solution of IPA and methyl isobutyl ketone (2:1 by volume) for 60 s at 21.0 °C. The PMMA on the ARC gratings was coated with gold palladium before measuring the stitching errors. Figure 4 shows the aligned gratings across the vertical and horizontal field boundaries.

The stitching precision was measured by comparing the spatial phase of the grating across the field boundaries as described by Ferrera *et al.*[8] Figure 6 shows histograms of the *x*- and *y*-stitching errors for vertical and horizontal boundaries. The mean errors, $\mu_{st}$, range from $-1.4$ to 2.5 nm and the standard deviations, $\sigma_{st}$, from 1.0 to 1.3 nm. Measuring the same grating pair 42 times yielded a standard deviation of 0.2 nm, so measurement uncertainty does not contribute significantly to the errors observed. In comparison, Raith specifies stitching precision for the system as 40 nm, mean $+2$ standard deviations. Our own evaluation of the system (open loop) revealed stitching errors between $\mu=-0.6$ nm, $\sigma=6.2$ nm, and $\mu=-15.4$ nm, $\sigma=9.1$ nm depending on location in the field.[15]

The Raith system does not guarantee global pattern placement, and the relative beam and stage positions were found

to drift ≈6 nm per minute without spatial-phase locking. The system drifts more rapidly until the sample and stage have thermally stabilized, and can drift more slowly under certain conditions.[15] In contrast, all patterns exposed using spatial-phase locking are positioned with respect to the fiducial grid. As a result, we can estimate overall pattern-placement errors from relative stitching measurements. If the placement errors of features on opposite sides of the field boundary are uncorrelated, then the pattern-placement precision, $\sigma_{pp}$, with respect to the grid, can be determined from the stitching precision, $\sigma_{st}$, i.e., $\sigma_{pp}=\sigma_{st}/\sqrt{2}\leqslant 0.9$ nm. Without spatial-phase locking, stitching measurements are not a reliable measure of global placement precision. The slow drifts described above may produce small stitching errors while at the same time accumulating large global placement errors.

## VI. CONCLUSIONS

The implementation of spatial-phase-locked electron-beam lithography with continuous feedback control has reduced stitching errors to the nanometer level on a low-cost scanning e-beam lithography tool. Spatial-phase locking overcomes the fundamental placement problems inherent in an open-loop beam-positioning system. In addition, the real-time system described here does not adversely impact throughput, and even eliminates the need to repeatedly reference fiducial marks. The use of a standard metrology grid that is replicated onto every substrate should eliminate placement variations between SEBL tools. When combined with a dose-modulating beam blanker and a fiducial grid suitable for manufacturing, SPLEBL will provide nanometer placement accuracy and improved throughput while reducing system-engineering and environmental-control costs.

## ACKNOWLEDGMENTS

The authors thank James Carter, James Daley, James Goodberlet, Mark Mondol, and Michael Walsh at MIT for their assistance. They also appreciate the help of Joe Klingfus and George Lanzarotta of Raith USA, and of Andreas Rampe of Raith GmbH. The development of spatial-phase-locked electron-beam lithography was supported by the DARPA Advanced Lithography Program and by ARO Grant No. DAAD19-99-1-0280.

[1] *International Technology Roadmap for Semiconductors* (Semiconductor Industry Association, San Jose, CA, 2002); http://public.itrs.net.
[2] J. N. Damask, V. V. Wong, J. Ferrera, H. I. Smith, and H. A. Haus, Proceedings of the Optical Fiber Communications Conference, 20–25 February 1994, Washington, DC, Optical Society of America.
[3] S. Mihailov, F. Bilodeau, O. Hill, D. Johnson, J. Albert, D. Stryckman, and C. Shu, IEEE Photonics Technol. Lett. **11**, 572 (1999).
[4] J. T. Hastings, M. H. Lim, J. G. Goodberlet, and H. I. Smith, J. Vac. Sci. Technol. B **20**, 2753 (2002).
[5] D. H. Dameron, C. C. Fu, and R. F. W. Pease, J. Vac. Sci. Technol. B **6**, 213 (1988).
[6] J. Ferrera, M. L. Schattenburg, and H. I. Smith, J. Vac. Sci. Technol. B **14**, 4009 (1996).
[7] C. G. Chen, P. T. Konkola, R. K. Heilmann, G. S. Pati, and M. L. Schattenburg, J. Vac. Sci. Technol. B **19**, 2335 (2001).
[8] J. Ferrera, V. Boegli, E. H. Anderson, D. P. Kern, and H. I. Smith, J. Vac. Sci. Technol. B **11**, 2342 (1993).
[9] J. Goodberlet, J. Ferrera, and H. I. Smith, J. Vac. Sci. Technol. B **15**, 2293 (1997).
[10] J. T. Hastings, F. Zhang, M. A. Finlayson, J. G. Goodberlet, and H. I. Smith, J. Vac. Sci. Technol. B **18**, 3268 (2000).
[11] A. Rampe, Raith GmbH private communication (2002).
[12] M. Gesley, D. Colby, F. Raymond, D. McClure, and F. Abboud, J. Vac. Sci. Technol. B **11**, 2378 (1993).
[13] S. Asai, H. Inomata, A. Yanagisawa, E. Takeda, I. Miwa, and M. Fukinami, J. Vac. Sci. Technol. **16**, 1710 (1979).
[14] M. Born and E. Wolf, *Principles of Optics: Electromagnetic Theory of Propagation, Interference and Diffraction of Light* (Cambridge University Press, New York, 1997).
[15] J. G. Goodberlet, J. T. Hastings, and H. I. Smith, J. Vac. Sci. Technol. B **19**, 2499 (2001).